Proceedings of Global Power and Propulsion Society
ISSN-Nr: 2504-4400
GPPS Shanghai25
September 4-6, 2025
www.gpps.global

GPPS-TC-2025-0060

Aerodynamic Investigation of Impingement/Effusion Double-Wall Cooling Using Time-Resolved Large Eddy Simulation (LES) Data

Riko Haase
Institute of Thermal Turbomachinery,
Karlsruhe Institute of Technology
riko.haase@kit.edu
Karlsruhe, Germany

Thomas Jackowski
Capgemini Engineering Deutschland S.A.S. & Co. KG
thomas@jackowski.de
Leinfelden-Echterdingen, Germany

Jonas Schmid
Institute of Thermal Turbomachinery,
Karlsruhe Institute of Technology
jonas.schmid@kit.edu
Karlsruhe, Germany

Hans-Jörg Bauer
Institute of Thermal Turbomachinery,
Karlsruhe Institute of Technology
hans-joerg.bauer@kit.edu
Karlsruhe, Germany

ABSTRACT

In this study the aerodynamics of an impingement/effusion double-wall cooling system is investigated. The focus of the analysis lies on the cavity between impingement plate and effusion plate. The aim is to gain a deeper understanding of the aerodynamics within this cavity and its influence on the cooling performance. Unsteady aerodynamic effects are evaluated by applying Proper Orthogonal Decomposition (POD) to the three-dimensional time-resolved velocity field.
The chosen setup consists of a regular pattern of cylindrical, wall-normal impingement holes and effusion holes with a 7-7-7 laidback fan-shaped geometry and 30-degree inclination angle, arranged in the same pattern and staggered to the impingement holes. Flow data are obtained by performing Large Eddy Simulation (LES). The resulting velocity field is validated against experimental results of stereoscopic particle image velocimetry measurements. The validation shows good agreement, particularly in the mean velocity field and the first POD mode. The analysis provides deep insight into the flow structure within the cavity of an impingement/effusion cooling setup, aiming to draw a connection between the unsteady behavior of the flow and the cooling performance.

INTRODUCTION

In modern jet engines, increasing turbine inlet temperatures is a key strategy for increasing thermal efficiency and thereby reducing CO_2 emissions. However, this approach challenges turbine and combustion chamber materials as the gas temperature often exceeds the materials' melting temperature. Effective cooling strategies are therefore essential to maintain performance and prolong turbine and combustion chamber lifetime. Schulz (2001) provides an overview of different cooling methods that are applied in combustor liners. He emphasizes that film cooling alone is insufficient to utilize the full cooling potential of the cooling air. Instead, it must be combined with convective cooling concepts, acting at the combustor liner's backside. Andrews et al. (1988) experimentally investigated one possible combination, the impingement/effusion cooling, and found that this combined impingement/effusion cooling significantly increases the heat transfer on the combustor liner's backside compared to impingement cooling alone. In an experimental study Martiny et al. (2000) compared impingement/effusion cooling with pure film cooling and showed that the effect of impingement cooling is particularly large in the upstream region at the beginning of the cooling film build-up, where the overall cooling effectiveness increased by around 15% compared to film cooling alone.
Based on these general observations, numerous studies were performed, varying different parameters in the impingement/effusion cooling setup. One frequently investigated parameter is the number of effusion holes relative to the impingement holes. Al Dabagh et al. (1990) and El-Jummah et al. (2017) both found that an equal number of impingement and effusion holes seems optimal, as a higher number of film cooling holes reduces the area with high wall parallel velocity near the effusion plate and thus the convective cooling. Niu et al. (2021) did a similar consideration but added coolant cross

flow to their experimental setup to increase the transferability to the real machine. The influence of the impingement and effusion plates distance to each other is examined by Cho and Rhee (2000). Additionally, they investigated the position of impingement and effusion holes relative to each other and found that a staggered arrangement is preferable compared to a shifted pattern. Xie et al. (2020) also draw the conclusion that a staggered hole arrangement is favorable compared to an arrangement with the effusion hole in alignment with the impingement hole. Another research focus is on the influence of crossflow within the cavity. This was considered by Rhee et al. (2003), Singh and Ekkad (2017) and Chen et al. (2019). Overall, it seems as strong crossflow leads to a decrease of heat transfer, while a moderate crossflow has little impact on the cooling performance.

The aforementioned studies cover a wide range of parameters of impingement/effusion cooling configurations. However, most of them focus primarily on the evaluation of overall cooling effectiveness and heat transfer. Optimized cooling, though, must be considered the result of optimized aerodynamics. Thus, to derive targeted improvements it is crucial to understand the aerodynamics within the cavity. Currently, only very few experimental studies acquire field velocity data within the cavity. Most numerical studies solve the Reynolds-averaged Navier-Stokes equations (RANS), which lack the temporal resolution required to capture unsteady effects and whose results are influenced by the choice of turbulence model and are therefore not always reliable. Only in a small number of studies the more reliable Large Eddy Simulation (LES) (Ammour and Page, 2017) or hybrid RANS-LES approaches (Andreini et al., 2018) were used. However, both studies analyze the unsteady flow behavior only to a very limited extent.

An unsteady analysis of the hot gas side of pure film cooling was done by Stichling et al. (2021) and Stichling and Bauer (2022) utilizing time-resolved data from stereoscopic particle image velocimetry (SPIV). By means of Proper Orthogonal Decomposition (POD) purely non-stationary vortex structures, namely shear vortex layer and wake vortices, were identified at the outlet of the film cooling hole. The unsteady behavior of pure impingement cooling was studied by Morsbach et al. (2024), who focused their POD analysis on the impingement jet itself. Furthermore, Shi et al. (2022) carried out an unsteady analysis of numerical data of tangential impingement jets by means of POD and extended POD and found a strong connection between coherent structures and heat transfer. However, Oguntade et al. (2017) compared impingement, effusion and impingement/effusion cooling, finding that the overall cooling effectiveness of the impingement/effusion setup was lower than predicted by evaluating the two cooling methods separately. This suggests that there is an aerodynamic interaction between both cooling methods and it is not sufficient to study impingement and effusion cooling separately. To fill this gap in research, based on the numerical study by (Jackowski et al., 2020) an impingement/effusion geometry was chosen to set up a new test rig for a comprehensive experimental investigation of impingement/effusion cooling. Infrared thermography was applied to examine the heat transfer characteristics (Jackowski et al., 2021b) and a first analysis of the aerodynamics within the cavity between impingement plate and effusion plate was done by means of SPIV (Jackowski et al., 2021a). In the extensive studies the cavity height as well as the relative position of impingement holes to effusion holes were varied and the mean flow field as well as the heat transfer characteristics were evaluated. However, an analysis of the unsteady flow behavior was done only to a very limited extent and due to the limitations of SPIV measurement technology, time-resolved data is only available for individual planes and not for the entire three-dimensional (3D) flow field.

The present study follows on from Jackowski et al. (2021a) and takes a closer look at the aerodynamics of one of the examined setups. By evaluating the unsteady aerodynamics within the cavity, the study seeks to identify the potential influence of the unsteady flow behavior on both the impingement and the effusion cooling. For this purpose, a 3D time-resolved velocity field is acquired using LES and validated against the SPIV data by Jackowski et al. (2021a). The mean velocity field is analyzed, and unsteady effects are investigated by applying POD to selected two- and three-dimensional sections of the domain.

METHODOLOGY

Numerical Setup

The configuration investigated with LES is adapted from the experimental setup examined by Jackowski et al. (2021a,b). The schematic of the test rig and the corresponding numerical setup are shown figure 1 (a) and figure 2 (a), respectively. Both setups consist of two channels, one for the coolant (1) and one for the hot gas (2). The two channels are connected with each other by impingement holes (3), through which coolant flows into the cavity (4). From there, the coolant enters the hot gas channel via the effusion holes (5). The configuration is characterized by the cavity height of $H = 5D$ where $D = 4mm$ is the impingement hole diameter. The pattern of impingement and effusion holes is shown in figure 1 (b) and 2 (b). The pitch is $P = 10D$ and the spacing is $S = 6.67D$. The impingement holes are located in the centers of each parallelogram that is built by the inlet of the effusion holes. While the impingement holes are cylindrical and wall-normal to the impingement plate, the effusion holes have a laidback fan-shaped 7-7-7 geometry as described by Schroeder and Thole (2014). The inclination angle of the effusion holes is 30° and the cylindrical part of the holes has a diameter of $E = \sqrt{2}D = 5.66mm$, which means that the cross sectional area of the effusion holes is two times higher than of the impingement holes. In the experimental setup the test specimen consists of 6 to 7 holes in lateral and 25 rows in longitudinal direction. In contrast, the numerical domain contains only three periods of the hole pattern in longitudinal and two periods in lateral direction (figure 2 (b)). In both directions a periodic approach is used, which is expected to be a good approximation for the middle area of the test

specimen. Thus, the considered areas of the impingement plate and the effusion plate are each $20D \times 20D$. Figures 2 (a) and (b) also show the coordinate system used in the following. The origin is at the center of the exit of one impingement hole and the x,y and z coordinates describes the longitudinal, lateral and wall-normal position, respectively.
The numerical simulations were carried out using the commercial software *Ansys Fluent 2023 R1*. LES is employed to solve the unsteady Navier-Stokes equations. To model the sub-grid turbulent kinetic energy (TKE) the wall-adapting local eddy-viscosity (WALE) turbulence model (Nicoud and Ducros, 1999) is used. The fluid is considered as compressible air under standard atmospheric conditions with a constant temperature of 298K, so the energy equation is not solved. Time advancement is based on the Courant-Friedrichs-Lewy (CFL) criterion and it is ensured that CFL<1 for the vast majority of cells.
For the mesh a hybrid approach with structured and unstructured parts is chosen. The impingement holes are meshed with a structured O-grid approach, while for the rest of the domain an unstructured grid with structured layers on the walls is used. It is ensured, that the most cells closest to the walls have a height of $y^+ < 1$. The grid is fine enough to resolve at least 80% of TKE in the whole domain, while for most parts of the cavity more than 90% are resolved. Overall, the grid consists of about 15 million cells.
As inlet conditions (figure 2 (a), red) for hot gas and coolant flow a block profile with a prescribed velocity is superimposed by turbulent fluctuations produced by the synthetic turbulence generator provided by Ansys Fluent (Shur et al., 2014). At the coolant inlet the velocity is set to match a Reynolds number of $Re_C = 4200$, where the impingement hole diameter D is used as length scale. The hot gas channel inlet velocity match $Re_H = 4000$. The turbulent intensity is 5% for both inlets. However, a sensitivity study showed that the inlet velocity magnitudes and profiles have relatively little influence on the flow structures within the cavity. The whole domain is considered as periodic in lateral direction and for the cavity also in longitudinal direction periodicity is assumed. To reduce the computational effort, only the upper half of the coolant channel is modeled and a symmetry condition is applied (yellow). For the same reason, the hot gas channel has been simplified as a plenum of $5D$ height with the inlet on the left and the outlet to the right and the top. All outlets (blue) are pressure outlets. At the coolant channel outlet an overpressure is applied, which leads to an impingement Reynolds number of $Re_{imp,LES} = 15274$, with D as characteristic length and and the mean velocity at the impingement hole exit as characteristic velocity. At all walls (grey) a no-slip condition is set.

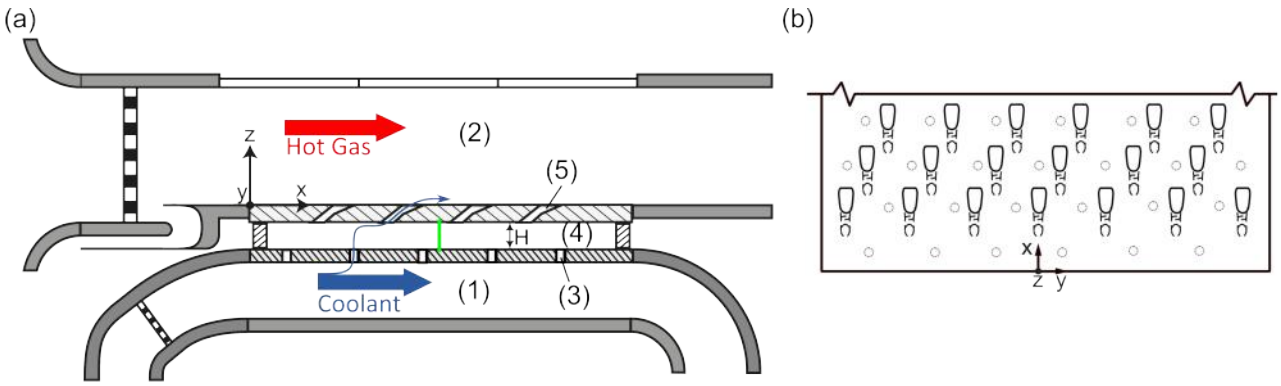

Figure 1 : (a): Test section with coolant channel (1), hot gas channel (2), impingement holes (3), cavity (4) and effusion holes (5) (Adapted from Jackowski et al. (2021a)). (b): Test arrangement of the cooling holes for effusion and impingement specimen (Adapted from Jackowski et al. (2021b)).

Experimental Methodology

To validate the LES results a test specimen with same geometrical pattern as as in the numerical setup is experimentally examined. The schematic setup is shown in figure 1. The hole pattern consists of 25 periods in x-direction and 6 periods in y-direction, so that the assumption of periodic boundary conditions made in the numerical setup is a good approximation for the area in the middle of the test specimen. The other boundary conditions are similar to those of the numerical setup. However, the resulting impingement Reynolds number is about 6% higher than in the numerical investigation.
The velocity field in the cavity of the test rig is measured with SPIV, which means that 2D3C (two dimensions, three components) time-resolved velocity data is gained. The measurement plane is parallel to to the y-z-plane as shown in green in figure 1 (a). By shifting the measurement plane in x-direction and assembling the planes to a volume a 3D time averaged velocity field is acquired. A detailed description of the facility infrastructure, the test rig and the measurement procedure is given by Jackowski et al. (2021a,b).

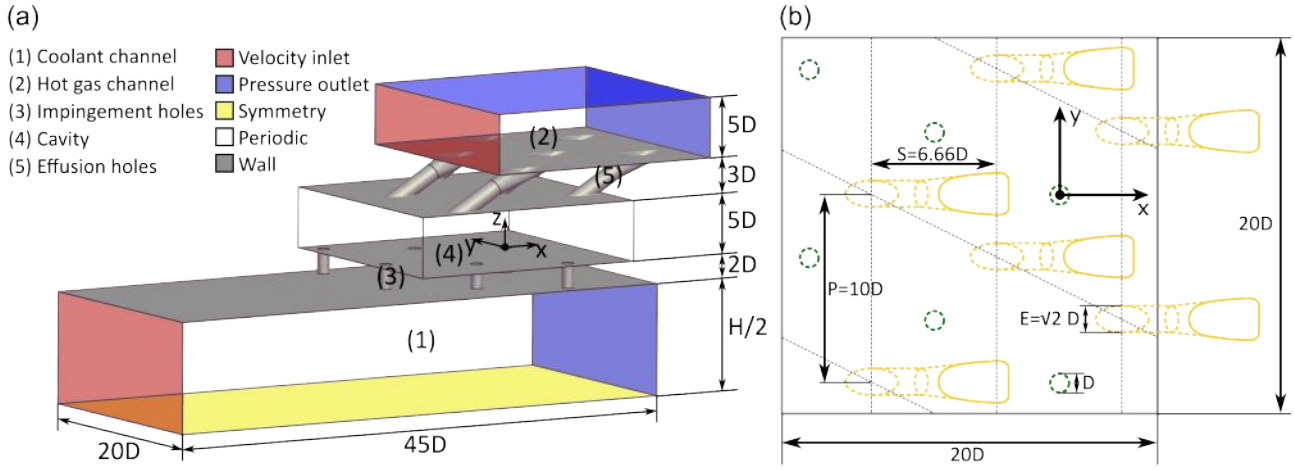

Figure 2 : Geometry of the numerical setup (a) and pattern of effusion and impingement holes (b).

Unsteady Analysis

For the unsteady flow analysis POD is applied to the time resolved flow fields. The computation is done with the snapshot POD following Weiss (2019), which is computationally more efficient than the direct POD if the number of grid points exceeds the number of snapshots. The POD is applied on a time series of the velocity fluctuation field $\vec{u}'(\vec{x},t)$ decomposing it into a set of linear independent spatial functions called modes $\vec{\phi}_k(x)$ modulated by the time coefficients $a_k(t)$:

$$\vec{u}'(\vec{x},t) = \sum_k a_k(t)\vec{\phi}_k(\vec{x}) \tag{1}$$

To obtain a set of linear independent modes the eigenvalue problem of the covariance matrix of the flatten velocity fluctuation field time series is solved. The resulting modes can be considered as coherent structures in the flow and its share of the total TKE corresponds to the related normalized eigenvalues. By taking into account only a limited number of modes a lower order model can be generated. For this, usually, the modes containing the most TKE are considered, which often corresponds to the modes describing large-scale flow structures. The time coefficients $a_k(t)$ of mode k are an indication how large the influence of the mode on the flow field is in a certain snapshot. In time average a_k is zero per definition, since the modes describe fluctuations. The more apart from zero a_k is the more active the mode. As indicated by equation 1, for negative values of a_k the direction of the mode reverses.
For the further analysis on how the modes influence the flow, a conditional averaging approach is used. This means that only snapshots fulfilling a certain condition are used to compute an averaged flow field. The conditions used in the following are that a_k is greater than one standard deviation of a_k ($\sigma(a_k)$) or a_k is smaller than minus one standard deviation of a_k, respectively. I.e., only snapshots are considered in which mode k is particularly active which helps to illustrate the effect the mode has on the flow field.

RESULTS AND DISCUSSION

LES Validation with SPIV Data

For the validation of the LES the SPIV data provided by Jackowski et al. (2021a) is used. Even though the overall pressure loss of the LES was defined by the boundary conditions and set to the value measured in the test rig, the resulting impingement Reynolds number $Re_{imp,LES} = 15274$ is slightly lower than experimentally evaluated. Therefore, to increase comparability the velocities shown in the following are normalized using the mean jet exit velocity u_{ref}.
To validate the LES results, in a first step the mean velocity fields are compared with the SPIV measurements. For the SPIV result the mean field is acquired by time averaging the single measurement planes and assembling the planes to a 3D field. For the LES data, due to the periodic boundary conditions in the cavity it is possible to gain mean quantities by averaging not only in time but also over the six periods of the pattern shown in figure 2 (b), which accelerates the convergence of the statistical variables. It is ensured that this type of averaging is permissible by comparing the averages of the single hole with each other as well. In figure 3 the mean velocity field resulting from the experimental setup (a) as well as the one resulting from the numerical setup (b) are shown. The selected window covers a section of the x-y-plane with a distance of $z/D = 4.5$ from the impingement plate. The position of the impingement hole is marked by a green dashed line and the inlet of the effusion holes is indicated by yellow dashed lines. The velocity direction and magnitude in the plane is indicated by the arrow direction and length. The magnitude of the plane normal velocity component is visualized by the coloring, where red indicates velocities towards the effusion plate and blue velocities towards the impingement plate. It is obvious that the highest velocities appear in the impingement jet, which has it main component normal to the depicted plane. Close

to the effusion wall the impingement jet is deflected into wall parallel direction, which is why the in-plane velocities are pointing away from the impingement jet. The negative w-velocity (blue area in figure 3) is caused by the interaction of the coolant with coolant from neighboring impingement jets, which leads to a stagnation of the wall-parallel flow and another deflection into negative z-direction. Thus, a hexagonal ring around the impingement jet forms which is only interrupted in the area of the effusion holes. Each of the rings can be considered as a hexagonal flow cell.

The unsteady behavior of the flow computed with LES is validated for the y-z-plane marked by the purple dashed line in figure 3. Figure 4 (a) shows the mean velocity field of this plane. The left column of the figure provides the experimental SPIV results and the right column the LES result. Again, the vectors indicate the velocity direction and magnitude in the plane and the coloring the plane normal velocity component. The green and yellow lines on the top and on the bottom of each sub-figure indicate the positions of the holes marked in figure 3. If the area between the bounds of the holes is filled, the hole lies within the shown plane, otherwise it is outside the plane. The flow fields shown in figure 4 (a) show a relatively good

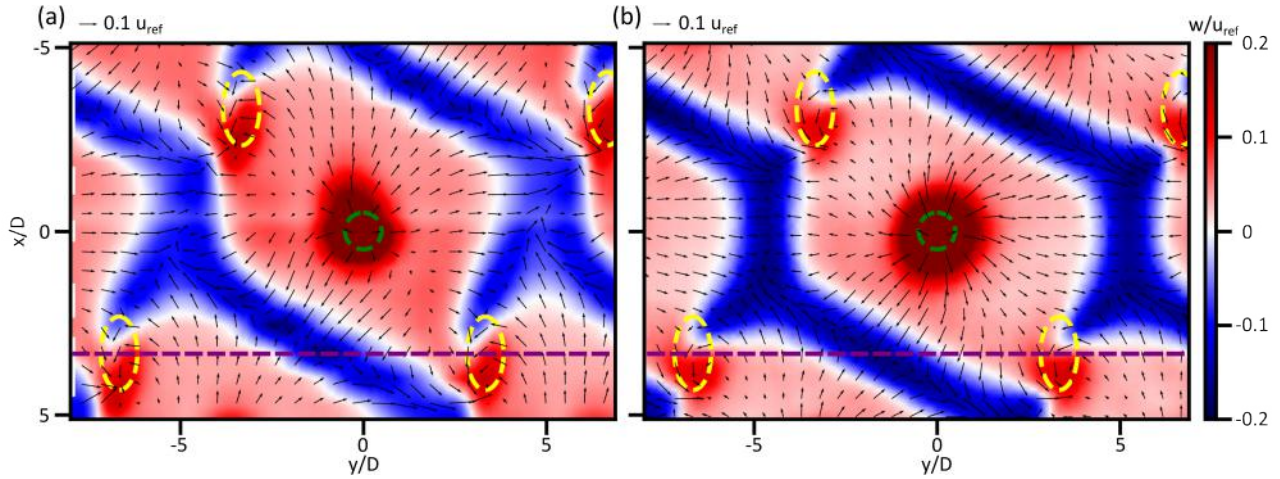

Figure 3 : Mean velocity field of the SPIV measurements (a) and the LES results (b) at a height of $z/D = 4.5$.

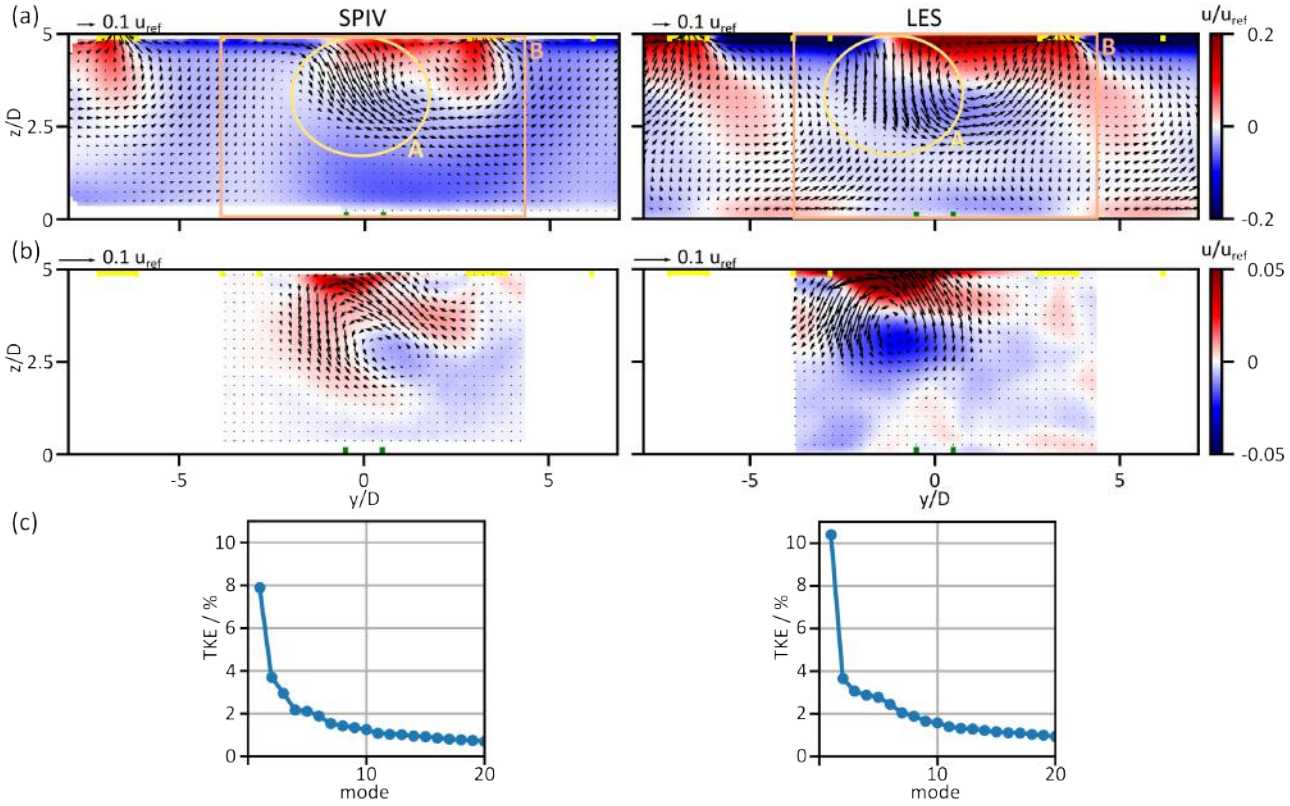

Figure 4 : Comparison of SPIV results (left) and LES results (right) at the y-z-plane indicated in purple in figure 3. (a): Mean velocity fields; (b): POD mode 1; (c): eigenvalue distribution

match between SPIV and LES for the in-plane velocity components. Though, considerable deviations are visible for the plane normal velocity component represented by the coloring. While the space averaged plane normal velocity component is close to zero in the LES, the same quantity is clearly negative in case of the SPIV indicating a crossflow inside the cavity. This crossflow in negative x-direction measured by SPIV is most likely a result of a discharge coefficient which is larger for the impingement holes further downstream than for the ones at the front of the plate due to a change of the incident flow of the impingement holes. Thus, mass flow and pressure loss through the single impingement holes are slightly varying in longitudinal direction which creates the crossflow in the cavity. This phenomenon cannot be captured by the simplified LES model since the cavity is periodic in longitudinal direction and contains only three rows of holes.
However, for the comparison of the mean kinetic energy in the plane shown in figure 4 (a) relatively good agreement is found. The calculation was done by computing the kinetic energy for each grid point and each time step and then averaging in time and space. For the given plane this results in a mean kinetic energy of $E_{kin}^{SPIV} = 0.00691\rho u_{ref}^2$ in the experiment and $E_{kin}^{LES} = 0.00759\rho u_{ref}^2$ for the LES. This can be explained by the fact that most of the kinetic energy comes from the structure created by the impingement jets, for which LES and PIV show good agreement. Also, the strong negative w-velocity indicating the border of a flow cell formed by the impingement jets is apparent around y/D=0 (marked with A in figure 4 (a)) in the SPIV as well as the LES results. This area of the flow should now be further examined by POD which is why window B of figure 4 (a) is chosen as the POD window. After applying the POD algorithm, the importance of the individual modes is assessed by the resulting normalized eigenvalue distribution shown in figure 4 (c), since the eigenvalue corresponds to the share of TKE a mode contains. The first POD mode covers 8% of the total TKE for the SPIV data and 10.5% for the LES data. For all further modes in both cases the amount of TKE is smaller than 4%. Accordingly, the following analysis concentrates on the first mode containing by far the most energy. Figure 4 (b) depicts the velocity fluctuation field associated with the first mode. To represent the mode's energy content, the field is multiplied by the standard deviation of the time coefficients corresponding to the mode. In both cases mode 1 is dominated by a vortex, which is centered around $y/D = 0$ for the SPIV data and is slightly shifted to the left in the LES case. Also, the effect the mode has, which is a shift in position and direction of the structure marked with A in figure 4 (a), is very similar. For the second mode (not shown) good agreement is found as well, while for higher modes LES and SPIV results diverge from each other. But since these higher modes describe structures of smaller scale and contain a much smaller share of the total TKE, it can be assumed that they have relatively little influence on the large-scale flow behavior. Thus, the following analysis of the LES results, which focuses on the large-scale flow structures, is not restricted by this. It can be concluded that the LES results coincide with the results from the SPIV measurement. At least qualitatively and up to a certain degree also quantitatively the mean velocity field and the first POD mode match well and the LES data can be used to further investigate the large-scale unsteady structures in the cavity.

3D Mean Velocity Field

To gain deeper insight into the complex flow within the cavity it is mandatory to investigate not only single cutting planes but also the whole 3d velocity field. For this purpose only the data gained with LES is used. Figure 5 (a) shows the isosurfaces of $w = 0.1u_{ref}$ (red) and $w = -0.1u_{ref}$ (blue), while figure 5 (b) shows an isosurface with a velocity magnitude of $|\vec{u}| = 0.25u_{ref}$. The yellow ellipses indicate the inlets of the effusion holes. Of course, the highest velocities occur within the impingement jet, which gets deflected into wall-parallel direction at the effusion wall. This leads to comparatively high wall parallel velocities close to the effusion wall, which is associated with a high convective heat transfer. However, as visible in figure 5 (b) there is a hexagonal ring where no velocities larger than $0.25u_{ref}$ occur close to the effusion wall. This is due to the interaction of neighboring impingement jets with each other as fluid from neighboring impingement jets meets in this area, which leads to stagnation of the velocity. This can be associated with a reduction of convective heat transfer in this region. Due to the stagnation of the wall-parallel velocity component, the flow is deflected into negative z-direction leading to the hexagonal pattern of the isosurface $w = -0.1u_{ref}$ depicted in figure 5 (a), which is only disrupted in the areas close to effusion holes.
For further investigation two cutting planes are defined by the windows (1) and (2) as indicated in figure 5. Both cuts go through the origin of the coordinate system defined in figure 2. While cut (2) simply represents a y-z plane, cut (1) is positioned in such a way that it passes through the impingement holes lying diagonally in a row (see figure 2) (b). The mean velocity fields of the two planes are shown in figure 6. In cut (1) two regions with a negative z-velocity component are visible (marked by the yellow rectangle), which occur due to the process described above. Thus, a vortex pair is forming with one clockwise rotating vortex left to the marked regions and one counter rotating vortex right so this region. Both vortices have a diameter of about 2.5D. However, the left vortex of the vortex pair is much more dominant than the right one, which does not appear to be completely closed. Similar, also in window (2) negative z-velocity component occur in the marked regions. The difference to cut (1), however, is that a more symmetric vortex pair is forming and the vortices have a diameter of the whole cavity height of 5D. This can be reasoned by the fact that in this direction the distance between neighboring impingement jets is larger giving the vortex pair more space to evolve.

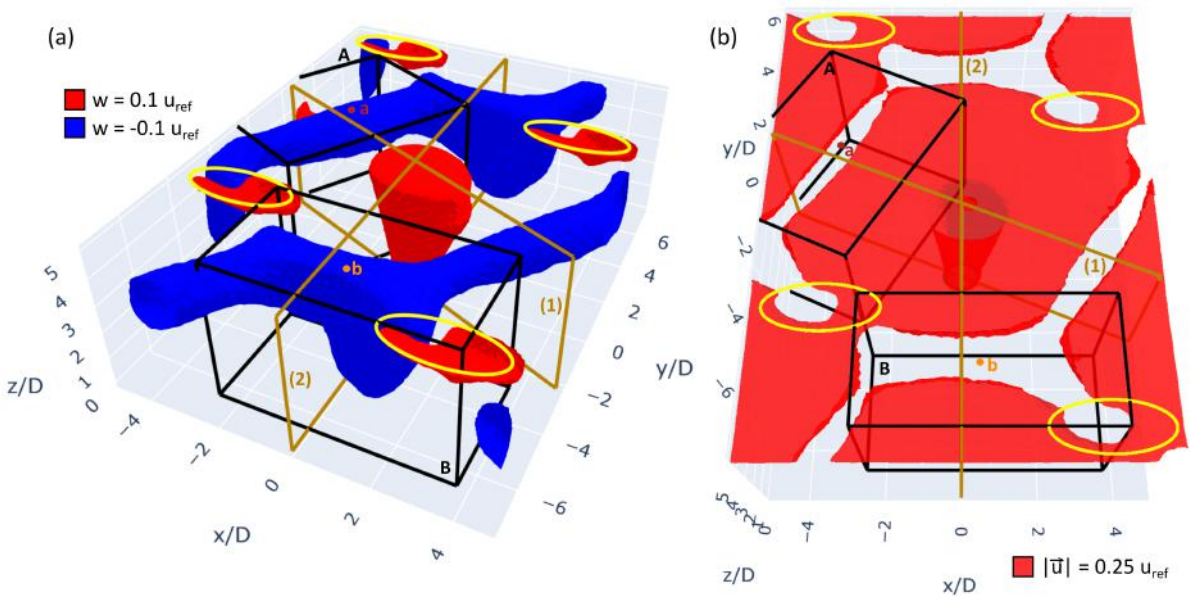

Figure 5 : Isosurfaces of the mean velocity field. (a): Isosurfaces with $\mathbf{w = -0.1u_{ref}}$ (blue) and $\mathbf{w = 0.1u_{ref}}$ (red). (b) Isosurface of $|\vec{u}| = \mathbf{0.25u_{ref}}$ (red).

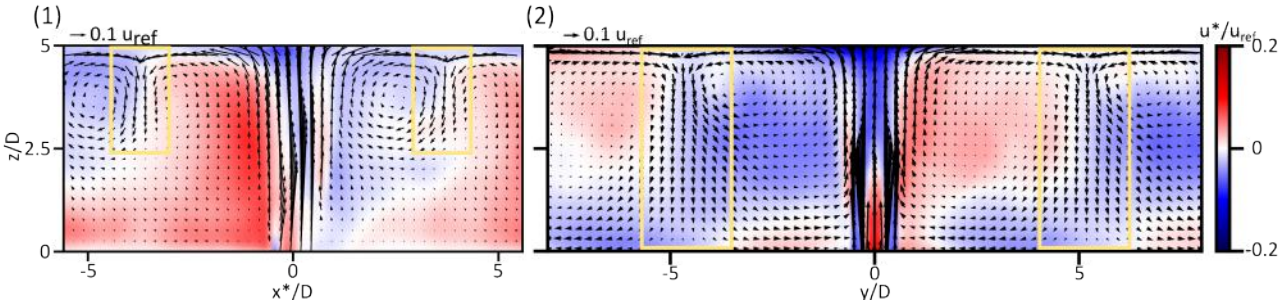

Figure 6 : Cut planes of the mean velocity field according to figure 5.

Unsteady Flow Behavior

For further investigation of the two different vortex structures found in the mean velocity field, the unsteady flow behavior is evaluated for two 3d sections marked by the cuboids A and B in figure 5. The sections are chosen since they cover the areas where the mean velocities close to the effusion wall are relatively small, from which a weak convective heat transfer can be expected. However, if large fluctuations in the velocity field occur there, high velocities can still be present at certain times, which could improve the heat transfer again. To evaluate this, POD is applied to the selected sections. From the eigenvalue distribution of the POD computed for section A (figure 7 (a)) it can be followed that the first mode is clearly dominant containing a share of 7.2% of total TKE and thus about 2.5 times more than the second most energetic mode. The first and second mode are shown in figure 8 (a) and (b) at a cut plane with $z = 4.5D$. The x*-y* coordinate system used here has its origin at one of the corners of cuboid A and is rotated to the x-y coordinate system as shown in figure 9 (a). Like before, the arrows indicate the flow direction and magnitude in the plane and the color provides the magnitude of the wall-normal velocity component. To increase comparability, the modes shown in figure 8 (a) and (b) are multiplied by the standard deviation of the corresponding time coefficients $\sigma(a_k)$. Mode 1 is dominated by a structure similar to the vortex seen in figure 4 (b) with the rotation axis along the y*-axis. Figure 8 (a) shows a cut parallel to the vortex rotation axis, and it becomes apparent that the expansion of the vortex in y*-direction covers the entire window length of 12D. In figure 8 (c) and (d) the conditionally averaged velocity fields for $a_1 > \sigma(a_1)$ and $a_1 < -\sigma(a_1)$, respectively, are depicted. From this it becomes apparent that the position of the area with negative z-velocity and stagnating wall-parallel velocity is influenced by mode 1. Depending on the magnitude of a_1 the area is shifted into negative (figure 8 (c)) or positive (figure 8 (d)) direction of x*. This shift is present over the entire length in y*-direction of the selected window. Defining the first mode as a kind of ground oscillation, mode 2 (figure 8 (b)) can be identified as the first harmonic, as it also describes a vortex with the rotation axis in y*-direction, but at about $y^*/D \approx 5-8$ the vortex changes its direction of rotation. This means that while the the area with negative z-velocity and stagnating wall-parallel velocity is shifted in one direction of x* for $y^*/D < 5$, it is shifted into the opposite direction for $y^*/D > 8$. Similarly, mode 4 can also be interpreted as a harmonic

of mode 1, while mode 3 mainly influences the expansion in x*-direction of the area with negative z-velocity.

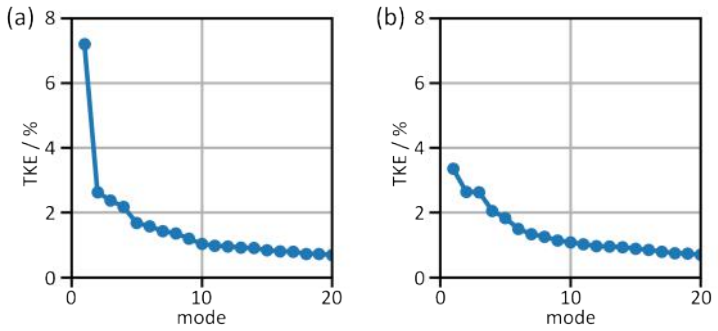

Figure 7 : Eigenvalue distribution of the POD computed for section A (a) and section B (b).

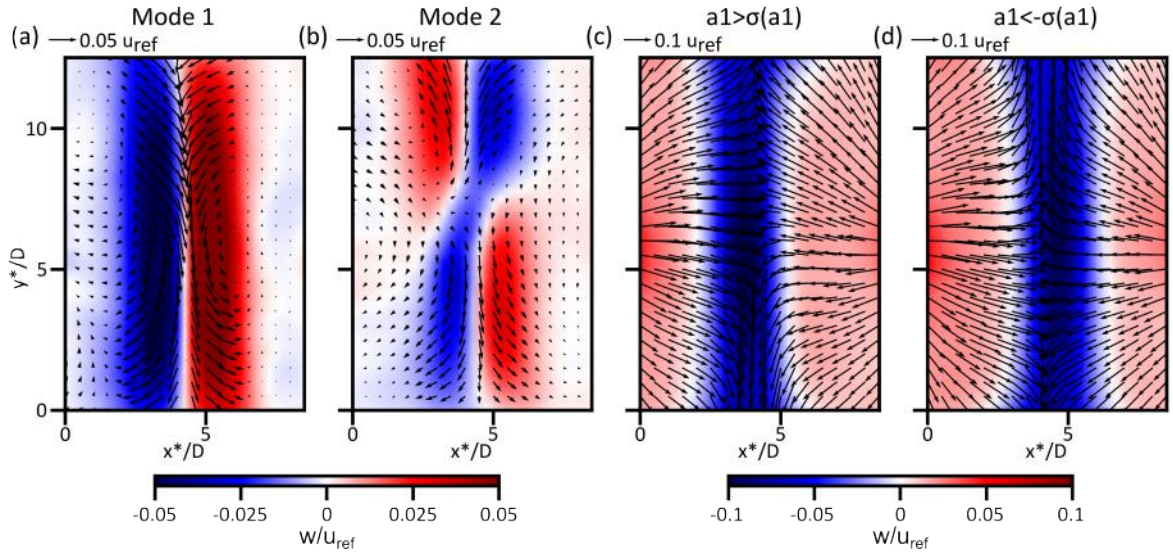

Figure 8 : POD modes 1 (a) and 2 (b) of section A of figure 5 and conditional averaging with $\mathbf{a_1} > \sigma(\mathbf{a_1})$ (c) and $\mathbf{a_1} < -\sigma(\mathbf{a_1})$ (d).

Applying the POD to section B does not deliver such a dominant first mode as indicated by the eigenvalue distribution of figure 7 (b). In fact, the first mode contains only 3.5% of the total TKE and thus not significantly more than the following modes. Additionally, the structures described by the first modes are found to be of much smaller scale than for section A. These two facts already indicate that the fluctuation have only little influence on the large-scale structures visible in the mean velocity field. This assumption is confirmed by applying the conditional averaging to the first mode of the POD computed for section A as well as for section B. Figure 9 (a) shows the isosurface of $\mid \vec{u} \mid = 0.25 u_{ref}$ of the conditionally averaged velocity field of section A. Averaging all snapshots where $a_1 > \sigma(a_1)$ (26% of all snapshots) results in the yellow isosurface and taking only the snapshots with $a_1 < -\sigma(a_1)$ (30% of all snapshots) gives the blue isosurface. Both isosurfaces are superimposed in the greenish region. The figure shows that the gap of the isosurface in section A of figure 5 (b) is completely filled by the two isosurfaces of the conditional averaged fields. Consequently, in section A relatively high velocities are present in all regions close to the effusion wall at least at certain times. In the same way the conditional averaging is applied to mode 1 of section B (figure 9 (b)), where the conditions are fulfilled by 22% ($a_1 > \sigma(a_1)$) and 26% ($a_1 < -\sigma(a_1)$) of all snapshots, respectively. It is apparent that mode 1 has only little influence on the flow and thus the two isosurfaces are only slightly shifted to each other. Therefore, the region of low velocity near the effusion wall in section B (figure 9 (b)) is not closed by the fluctuations described by mode 1. The resulting isosurfaces of the conditional averaging of the further modes look very similar to those of the first mode and these modes do not have a significant influence on this region of low velocity either. From this, it can be concluded that the area with low velocity in section B is much more stable in position than in section A. This investigation is confirmed by comparing the magnitude of the velocity fluctuations $|\vec{u}'|$ for the two exemplary points marked with a and b in figure 5. Both points have a distance to the effusion wall of $0.125d$. For a period of time of $50t_{ref}$, where $t_{ref} = d/u_{ref}$, the time history of the magnitude of the velocity fluctuation is shown in figure 10 (a). Compared to point b, in point a the fluctuations are larger. This can be also seen by comparing the turbulent kinetic energy, which is $TKE_a = |\vec{u}'(a)|^2 = 0.0431 u_{ref}^2$ in point a and $TKE_b = 0.0235 u_{ref}^2$ in point b. How the single modes

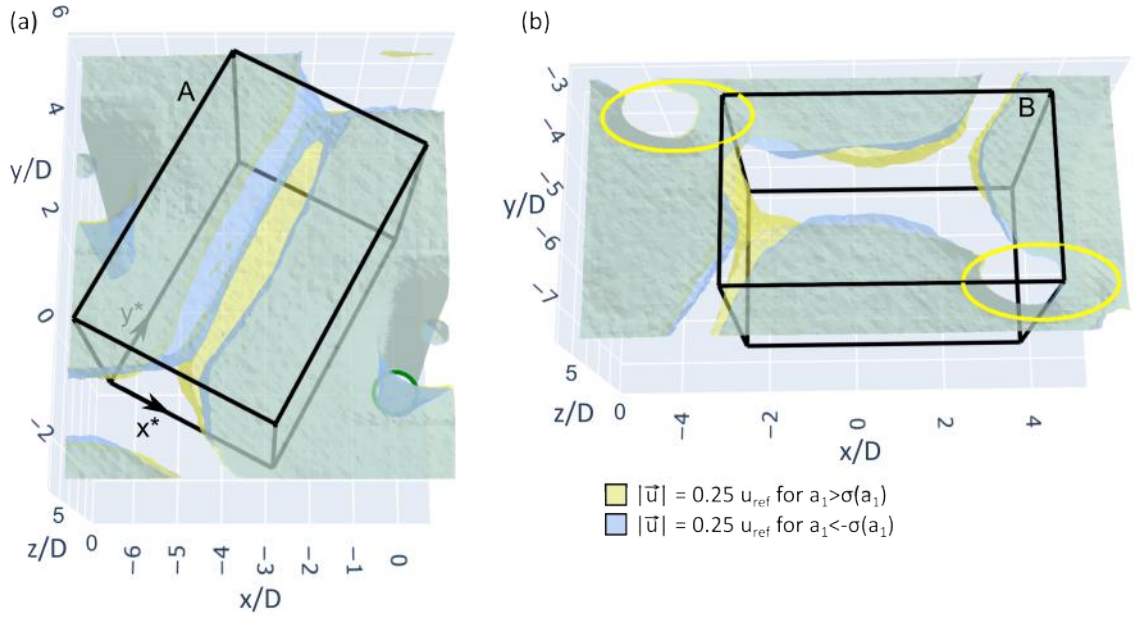

Figure 9 : Isosurfaces of the velocity magnitude $|\vec{u}| = 0.25\mathbf{u_{ref}}$ from the conditionally averaged flow fields with $\mathbf{a_1} > \sigma(\mathbf{a_1})$ (yellow) and $\mathbf{a_1} < -\sigma(\mathbf{a_1})$ (blue) for the PODs computed for section A (a) and B (b).

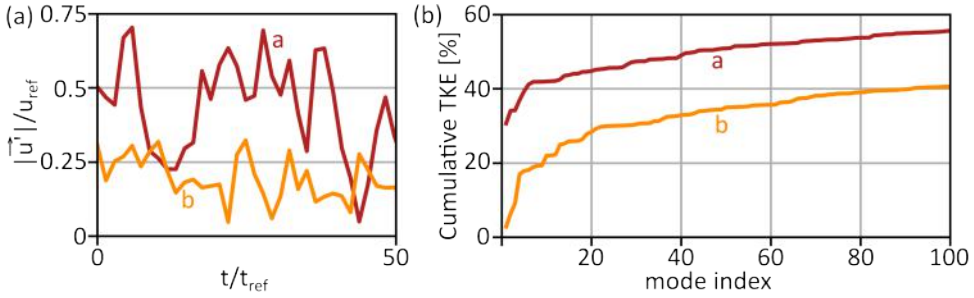

Figure 10 : (a) Time history of the magnitude of the velocity fluctuations for the two points a and b marked in figure 5. (b) Cumulative contribution of the single modes to the TKE in points a and b marked in figure 5.

contribute to the TKE in these points is shown in figure 10 (b) where the cumulative share of the modes to the total TKE is shown for both points. For point a the first mode contains already about 31% of the TKE and 44 modes are necessary to capture half of the kinetic energy. In point b the share of covered TKE increases more gradually with the number of modes taken into account and the first 100 modes contain only roughly 40% of the TKE. This supports the statement made before that in region A highly energetic unsteady structures are present close to the effusion wall, while this is not the case for section B. Thus, the flow pattern in region A is more stable than in region B. One possible reason for this is that section B has a larger distance to the impingement jets. Therefore, it is less strongly influenced by the fluctuations of the impingement jet and the structures have more space to evolve (see figure 6), which could also increase their stability. The second possible explanation is that section B is closer to the effusion holes and the suction effect that emanates from them possibly can have a stabilizing effect on the flow.

Regardless of the cause, the stability of the flow structures can have an important influence on the convective heat transfer. To examine this influence, in figure 11 (a) the Nusselt number distribution on the backside of the effusion wall is shown. The data is computed from infrared thermography measurements on the corresponding experimental test rig and was first published by Jackowski et al. (2021b). The impingement diameter D is used as characteristic length scale. The distribution reveals that in section A the Nusselt number in the areas with low mean velocities close to the effusion wall (see figure 5) is significantly higher than the corresponding area of section B For a quantitative comparison, figure 11 also shows the curve of the Nusselt numbers along the axes x_A and x_B (b) as well as y_A and y_B (c) as marked in sub-figure (a). The higher Nusselt numbers of section A compared to section B can be reasoned by the fact that in the less stable section A larger fluctuations are present. Thus, relatively high velocities occur in all regions close to the effusion wall at least at certain times, even though the time averaged velocity is low in some areas. This leads to an increase of the time averaged Nusselt number. In contrast, the flow structure of section B is more stable, which means that the fluctuating part of the velocities has less influence on the heat transfer. Thus, in the areas of low mean velocities, also the Nusselt number is small. From this

investigation it can be followed that the fluctuating part of the velocity field influences the convective heat transfer and thus the cooling. Therefore, it seems to be useful to take these unsteady effects into account, especially if the spatial distribution of a cooling parameter is considered.

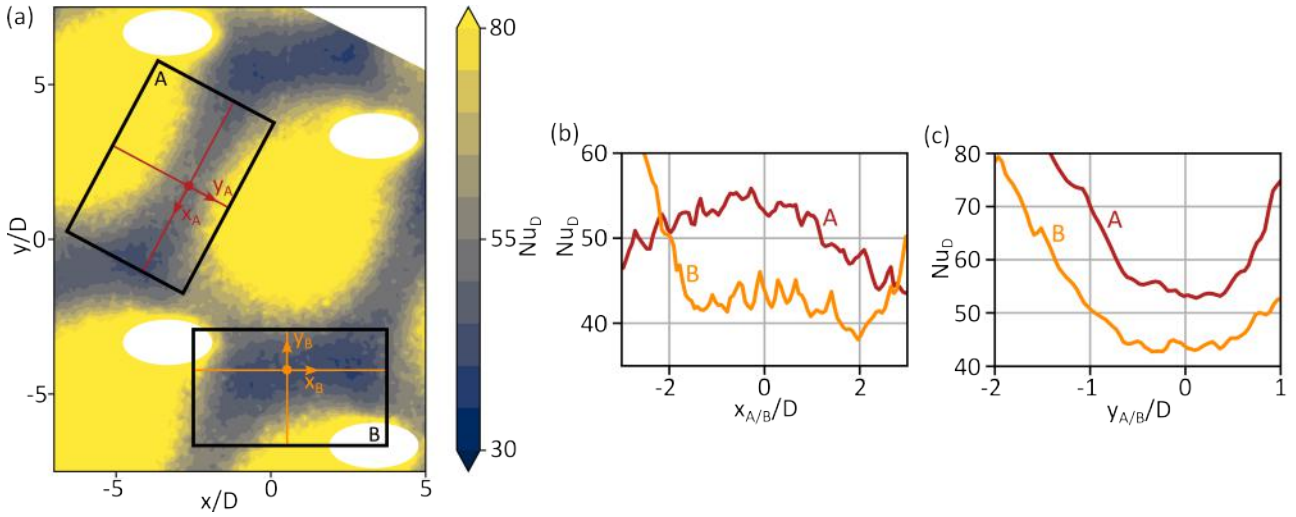

Figure 11 : Nusselt number distribution on the backside of the effusion wall (a) and curves of the Nusselt number along the axes x_A and x_B (b) as well as y_A and y_B (c). (Data was first published by Jackowski et al. (2021b).)

CONCLUSIONS

The aerodynamics within the cavity of a double-wall impingement/effusion cooling system was investigated by LES. The cavity height was chosen to 5D and the effusion holes are staggered to the impingement holes. The impingement Reynolds number of the considered case is $Re_{imp} = 15274$ and the acquired velocity field was validated against experimental data obtained with SPIV measurements. The following conclusions can be drawn from the numerical study:

1. The mean velocity field of the LES is in good agreement to the experimentally measured field. For a selected 2D window also unsteady LES and SPIV data were compared by means of POD. The LES shows good agreement to the SPIV measurements in the first two modes, which define unsteady large-scale structures of the flow.

2. The 3D velocity fields computed with LES indicate that the flow in the cavity is very complex and three dimensional. The flow consists of hexagonal flow cells each containing an impingement jet in the center. However, the flow is highly unsteady, especially in the intersection area of two neighboring flow cells.

3. POD of two selected 3D sections of the domain reveals that there are huge area-dependent differences in the unsteady aerodynamics. In the regions between neighboring impingement holes, the flow is dominated by unsteady effects. In contrast, near the effusion holes, the flow is much more stable and large-scale unsteady structures play only a minor role. These differences in unsteady flow behavior can be linked to the spatial distribution of convective heat transfer on the effusion wall, where higher fluctuations are associated with an increased convective heat transfer.

Overall, the study shows that an unsteady flow analysis is mandatory to obtain a comprehensive understanding of the flow within the cavity of impingement/effusion cooling setups. The unsteady flow behavior can be directly linked to certain phenomena visible in the convective heat transfer. However, to evaluate how the effects shown depend on the chosen setup, further studies varying geometric parameters and flow boundary conditions are mandatory.

NOMENCLATURE

Symbols

σ	Standard deviation
$\vec{\phi}_k$	POD mode number k
a_k	Time coefficients of POD mode number k
D	Impingement hole diameter
t	time
u, v, w	velocity components
u_{ref}	impingement jet exit velocity
x, y, z	spatial coordinates

Abreviations

3D	Three-dimensional
LES	Large Eddy Simulation
POD	Proper Orthogonal Decomposition
RANS	Reynolds-averaged Navier-Stokes
SPIV	Stereoscopic particle image velocimetry
TKE	Turbulent kinetic energy

ACKNOWLEDGMENTS

The research leading to the results presented in this paper is supported by the Deutsche Forschungsgemeinschaft (DFG project number 517489232). This financial support is gratefully acknowledged. The responsibility of the content lies solely with the authors.

REFERENCES

References

Al Dabagh, A. M., Andrews, G. E., Abdul Husain, R. A. A., Husain, C. I., Nazari, A. and Wu, J. (1990), 'Impingement/effusion cooling: The influence of the number of impingement holes and pressure loss on the heat transfer coefficient', *Journal of Turbomachinery* **112**(3), 467–476.

Ammour, D. and Page, G. J. (2017), Modelling impingement-effusion flow inside double-walled combustor tile, *in* 'Volume 5B: Heat Transfer', GT2017, American Society of Mechanical Engineers.

Andreini, A., Cocchi, L., Facchini, B., Mazzei, L. and Picchi, A. (2018), 'Experimental and numerical investigation on the role of holes arrangement on the heat transfer in impingement/effusion cooling schemes', *International Journal of Heat and Mass Transfer* **127**, 645–659.

Andrews, G. E., Asere, A. A., Hussain, C. I., Mkpadi, M. C. and Nazari, A. (1988), Impingement/effusion cooling: Overall wall heat transfer, *in* 'Volume 4: Heat Transfer; Electric Power; Industrial and Cogeneration', GT1988, American Society of Mechanical Engineers.

Chen, G., Liu, Y., Rao, Y., He, J. and Qu, Y. (2019), 'Numerical investigation on conjugate heat transfer of impingement/effusion double-wall cooling with different crossflow schemes', *Applied Thermal Engineering* **155**, 515–524.

Cho, H. H. and Rhee, D. H. (2000), 'Local heat/mass transfer measurement on the effusion plate in impingement/effusion cooling systems', *Journal of Turbomachinery* **123**(3), 601–608.

El-Jummah, A. M., Nazari, A., Andrews, G. E. and Staggs, J. E. J. (2017), Impingement/effusion cooling wall heat transfer: Reduced number of impingement jet holes relative to the effusion holes, *in* 'Volume 5C: Heat Transfer', GT2017, American Society of Mechanical Engineers.

Jackowski, T., Elfner, M. and Bauer, H.-J. (2020), Numerical investigation of conjugate heat transfer in an effusion and impingement cooled combustor wall, *in* 'GT2020'.

Jackowski, T., Elfner, M. and Bauer, H.-J. (2021b), 'Experimental study of impingement effusion-cooled double-wall combustor liners: Thermal analysis', *Energies* **14**(16), 4843.

Jackowski, T., Elfner, M., Bauer, H.-J., Stichling, K. and Hahn, M. (2021a), 'Experimental study of impingement effusion cooled double-wall combustor liners: Aerodynamic analysis with stereo-piv', *Energies* **14**(19), 6191.

Martiny, M., Schulz, A. and Wittig, S. (2000), Effusion cooled combustor liners of gas turbines—an assessment of the contributionsof convective, impingement, and film cooling, *in* 'In Proceedings of the Symposium on Energy Engineering in the 21st Century (SEE2000)', pp. 221–228.

Morsbach, C., Matha, M., Brakmann, R. G., Tabassum, S., Bergmann, M., Schroll, M., Willert, C. and Kügeler, E. (2024), Investigating the unsteady dynamics of a multi-jet impingement cooling flow using large eddy simulation, *in* 'Volume 8: Heat Transfer: Internal Air Systems; Heat Transfer: Internal Cooling; Industrial and Cogeneration', GT2024, American Society of Mechanical Engineers.

Nicoud, F. and Ducros, F. (1999), 'Subgrid-scale stress modelling based on the square of the velocity gradient tensor', *Flow, Turbulence and Combustion* **62**(3), 183–200.

Niu, J.-j., Liu, C.-l., Liu, H.-y., Xiao, X. and Lin, J.-f. (2021), 'Theoretical and experimental analysis of overall cooling effectiveness for afterburner double-wall heat shield', *International Journal of Heat and Mass Transfer* **176**, 121360.

Oguntade, H. I., Andrews, G. E., Burns, A. D., Ingham, D. B. and Pourkashanian, M. (2017), Impingement/effusion cooling with low coolant mass flow, *in* 'Volume 5C: Heat Transfer', GT2017, American Society of Mechanical Engineers.

Rhee, D. H., Choi, J. H. and Cho, H. H. (2003), 'Flow and heat (mass) transfer characteristics in an impingement/effusion cooling system with crossflow', *Journal of Turbomachinery* **125**(1), 74–82.

Schroeder, R. P. and Thole, K. A. (2014), Adiabatic effectiveness measurements for a baseline shaped film cooling hole, *in* 'Volume 5B: Heat Transfer', GT2014, American Society of Mechanical Engineers.

Schulz, A. (2001), 'Combustor liner cooling technology in scope of reduced pollutant formation and rising thermal efficiencies', *Annals of the New York Academy of Sciences* **934**(1), 135–146.

Shi, L., Zhu, X. and Du, Z. (2022), The heat transfer and coherent structures of the tangential impingement jets in the annular chamber studied with extended proper orthogonal decomposition, *in* 'Volume 6B: Heat Transfer — General Interest/Additive Manufacturing Impacts on Heat Transfer; Internal Air Systems; Internal Cooling', GT2022, American Society of Mechanical Engineers.

Shur, M. L., Spalart, P. R., Strelets, M. K. and Travin, A. K. (2014), 'Synthetic turbulence generators for rans-les interfaces in zonal simulations of aerodynamic and aeroacoustic problems', *Flow, Turbulence and Combustion* **93**(1), 63–92.

Singh, P. and Ekkad, S. V. (2017), 'Effects of spent air removal scheme on internal-side heat transfer in an impingement-effusion system at low jet-to-target plate spacing', *International Journal of Heat and Mass Transfer* **108**, 998–1010.

Stichling, K. and Bauer, H.-J. (2022), Aerothermal analysis of film cooling flows, *in* 'Proceedings of the 25th ISABE Conference, Ottawa, CAN, September 25-30, 2022'.

Stichling, K., Elfner, M. and Bauer, H.-J. (2021), 'Investigation of film cooling using time-resolved stereo particle image velocimetry', *Journal of Turbomachinery* **143**(7).

Weiss, J. (2019), 'A tutorial on the proper orthogonal decomposition', *AIAA Aviation 2019 Forum* .

Xie, G., Liu, C.-l., Ye, L., Wang, R., Niu, J. and Zhai, Y. (2020), 'Effects of impingement gap and hole arrangement on overall cooling effectiveness for impingement/effusion cooling', *International Journal of Heat and Mass Transfer* **152**, 119449.